Influence of pretreatment on the properties of α-Fe$_2$O$_3$ and the effect on photocatalytic degradation of methylene blue under visible light

S. Mokhtari, N. Dokhan, S. Omeiri, B. Berkane and M. Trari

ABSTRACT

The hematite (α-Fe$_2$O$_3$) nanostructures were synthesized by thermal oxidation of metal at 500 °C under atmospheric pressure. We studied the effect of the electrochemical pretreatment of the substrate before calcinations and its impact on the morphology, crystalline structure, lattice microstructural, and optical properties of α-Fe$_2$O$_3$. Uniform nanosheets were observed on the sample surface after calcination; their dimension and morphology were accentuated by the pretreatment, as confirmed by the SEM images. The characteristics of the nanostructures, analyzed by X-ray diffraction (XRD), revealed a rhombohedral symmetry with the space group R-3c and lattice constants: a = 0.5034 nm and c = 1.375 nm. The average crystallite size and strain, determined from the Williamson-Hall (W-H) plot, showed substantial variations after the substrate pretreatment. The Raman spectroscopy confirmed the changes in the crystal properties of the hematite submitted to pretreatment. The diffuse reflectance allowed to evaluate the optical gap which lies between 1.2 and 1.97 eV, induced by the electrochemical processing. The photocatalytic activity of α-Fe$_2$O$_3$ films was assessed by the degradation of methylene blue (MB) under LED light; 15% enhancement of the degradation for the pretreated specimens was noticed.

Key words | electrochemical pretreatment, hematite nanosheets, kinetic model, microstructural analysis, photocatalysis, thermal oxidation

S. Mokhtari
N. Dokhan (corresponding author)
B. Berkane
Research Unit, Materials, Processes and Environment (URMPE), University M'Hamed Bougara,
Boumerdes,
Algeria
E-mail: *nahed.dokhan@univ-boumerdes.dz*

S. Omeiri
M. Trari
Laboratory of Storage and Valorization of Renewable Energies, Faculty of Chemistry (USTHB),
BP 32, 16111 Algiers,
Algeria

HIGHLIGHTS

- Hematite nanosheets were synthesized by thermal oxidation of iron foils.
- An electrochemical pretreatment before oxidation was investigated and then compared to the results without pretreatment.
- Pretreatment affects several properties of the α-Fe$_2$O$_3$ nanosheets (morphological, microstructural, optical and electrochemical).
- Pretreatment was found to improve the photocatalytic activity of the hematite nanosheets.

INTRODUCTION

Currently, energy and environmental needs are directing research toward compounds preferably made up of abundant, inexpensive, and non-toxic elements in order to obtain materials with interesting functionalities that can be produced by reliable and clean methods on an industrial scale (Lewis & Nocera 2006). This investigation is a contribution to thin films through the attempt to improve the properties of hematite nanostructures. Stoichiometric hematite (α-Fe$_2$O$_3$) is a narrow band gap semiconductor with a red color. It most generally occurs in n-type (Sivula *et al.* 2011; Elda *et al.* 2017) and its physical properties depend on the preparative conditions (Cornell &

Schwertmann 2003). The optical gap is between 1.9 and 2.2 eV, depending on the synthesis method and such band gap allows it to absorb ~30% of solar light. Moreover, the hematite is the most stable iron oxide in the binary system Fe-O, and it shows a good stability against dissolution over a wide pH range (pH > 4) owing to its basic character (Cornell & Schwertmann 2003), in addition to its availability and easy elaboration. α-Fe$_2$O$_3$ is widely used in magnetic recording and in the medical field; the nanostructures prove to have various applications in many fields such as Li-ion batteries and gas sensors (Sun *et al.* 2010), photoanodes for dye solar cells, water splitting and photodegradation of pollutants (Chirita & Grozescu 2009).

For photocatalytic applications, an ideal material must be stable, inexpensive, non-toxic and possess an appreciable photoactivity (Chirita & Grozescu 2009). Hematite largely satisfies these conditions and intensive research has been carried out to assess its photocatalytic efficiency, primarily through adequate engineering of the solid-liquid junction. With a clear understanding of the underlying mechanisms of absorption of photons to final catalytic reactions. The hematite is characterized by a short diffusion length (2–4 nm) and a high recombination rate of photoinduced electron-holes (e$^-$/h$^+$). Researches on α-Fe$_2$O$_3$ focus on the elaboration of nanostructures in the forms of nanosheets, nanowires, nanocrystals, etc., to improve the catalytic performances by ensuring good charge transfer, thus minimizing the recombination rate and increasing the electrical conductivity. Hence, it is largely preferable to use nanostructures with a low thickness to allow the photogenerated charge carriers to reach the liquid interface before their recombining and to contribute to photo redox reactions. In addition, nanostructures offer more semiconductor-liquid contact surface while increasing light harvesting (Steier *et al.* 2014).

Several techniques are currently used to synthesize nanostructured hematite such as chemical vapor deposition, the hydrothermal route, chemical precipitation, the sol-gel method, electrochemical anodization, pulsed laser deposition (Elda *et al.* 2017) and thermal oxidation of iron (Wen *et al.* 2005). The latter is simple and low cost and can take place under various oxidizing atmospheres. The morphology of the nanostructures and the properties can be modulated by modifying the experimental conditions during oxidation (Wen *et al.* 2005). Thermal oxidation can be done on iron sheets (Yuan *et al.* 2013) or onto thin iron films (Hiralal *et al.* 2011); it can be realized in a furnace (Yuan *et al.* 2013), on a hot plate (Hiralal *et al.* 2011) or by passing a strong electric current through iron wires

(Nasibulin *et al.* 2009). Many factors can influence the characteristics of thermally developed oxides. Among these factors, surface pretreatment is the one whose effect is most often underestimated. Reports related to the surface preparation effects on thermally oxidized iron are not abundant, most date back between 1947 and 1997 (Bénard & Coquelle 1947; Graat *et al.* 1997) and clearly showed the significant influence of surface pretreatment on the oxidation rate and oxide properties. Since the advent of nanotechnology in the last two decades, we have not found works really dedicated to the study of the pretreatment effects on the properties of iron oxide nanostructures obtained by thermal oxidation. In this work, we try to fill this gap by investigating the effect of electrochemical pretreatment, in comparison with the classical cleaning process, on the properties of hematite nanosheets.

EXPERIMENTAL

The synthesis of α-Fe$_2$O$_3$ nanosheets was carried out by oxidation in air at 500 °C during 2 h for both protocols. Iron sheets (99.5% purity, Good Fellow 0.1 mm × 5 mm × 18 mm) were used as substrates. The samples were divided into two categories. In the first one, the samples were submitted only to cleaning procedure before treatment (protocol a), consisting of immersing the samples in an ultrasonic bath successively in acetone (10 min), ethanol (10 min), distilled water (10 min), and finally drying with hot air (~45 °C). In the second protocol (b), the samples were submitted to an electrochemical pretreatment (0.5 M H$_2$SO$_4$, 6 V, 5 min, Fe anode, Pt cathode) followed by the same cleaning procedure. The thermal annealing is carried out at 500 °C at a heating rate of 15 °C/min under an air humidity of 65%.

The crystalline phase was confirmed by X-ray diffraction (XRD) using a Panalytical X'Pert diffractometer with a copper anticathode ($\lambda = 1.540598$ Å) in the 2θ range (20–80°). The surface morphology of the films was characterized by Environmental Scanning Electron Microscope (ESEM) Philips XL30 at 20 kV using secondary electron mode (SE). The Raman spectroscopy Horiba LabRAM HR (633 nm He-Ne laser,700 μW) was used for analyzing the different phonon modes of the hematite. The diffuse reflectance spectrum was plotted in the range (200–800 nm) with a Jasco V-530 spectrophotometer equipped with an MgO-coated integrating-sphere, the diffuse part of the reflected light was collected. The Mott–Schottky characteristics were plotted in alkaline solution (NaOH, 0.5 M) in a standard

electrochemical cell containing the working electrode, Pt auxiliary electrode and a saturated calomel electrode (SCE).

PHOTOACTIVITY

The photocatalytic study was performed on the films (4 cm^2) irradiated by a LED lamp (20 W), emitting mainly in the visible region with a maximum at 520 nm. The distance between the reactor containing the MB solution and the light source was fixed at 5 cm, providing a flux of 26 mW cm^{-2}, and the film is immersed horizontally. All experiments were conducted at room temperature. Typically, a piece of a sample made up of the as-grown hematite on iron foil (Fe/Fe$_2$O$_3$) was put in a Pyrex beaker containing 30 mL of MB (4.0 ppm). The solution was left in the dark for 60 min for adsorption equilibrium of MB on the samples before illumination. Aliquots (3 mL) were withdrawn from the reaction solution at regular times (20 min), and the MB concentration was measured with a Shimadzu UV-2550 spectrophotometer according to Beer Lambert's law. The absorption of the solution was determined by linear interpolation of a calibration curve.

RESULTS AND DISCUSSION

SEM analysis

Figure 1 shows the surface morphologies of the films treated with protocols (a) and (b). One can see that the electrochemical pretreatment significantly affects the morphology of the grown film. Nanosheets were formed on both surfaces,

we can notice that in the image corresponding to protocol (a) (Figure 1 left) the nanosheets are smaller and numerous while those of protocol (b) (Figure 1 right) are larger and well separated with almost flat spaces.

According to the SEM analysis, we can presume that with protocol (a), the nucleation and growth of nanosheets continue to occur during the entire annealing step; this is not the case for protocol (b) where large nanosheets preferably develop during annealing, giving rise to a reduced amount of new nucleated nanostructures. This result can be linked to the predominance of the grain-boundary diffusion over the lattice diffusion for protocol (b) because the former particularly favors the development of protuberances in the superficial film, inducing different types of nanostructures.

XRD analysis

Figure 2 shows the XRD patterns of α-Fe$_2$O$_3$ annealed after processing with protocols (a) and (b). All peaks are indexed in a rhombohedral symmetry (space group: R-3c), in agreement with the JCPDS Card N° 33-0664, indicating a good crystallinity with lattice constants $a = 0.5034$ nm and $c = 1.375$ nm. α-Fe$_2$O$_3$ has three predominant peaks (110), (214) and (104); a small amount of magnetite (Fe$_3$O$_4$) is also detected as a secondary phase (2θ 43.51° and 56.87°, JCPDS Card N° 96-900-9769).

The peak (110) presents stronger intensity for the hematite elaborated with protocol (a), indicating that under conventional cleaning a higher amount of crystallite grows with the (100) planes parallel to the substrate surface. We also observe a clear appearance of the peak (012), not clearly distinguished in protocol (b). Moreover, a slight shift to lower angles is observed for samples treated by
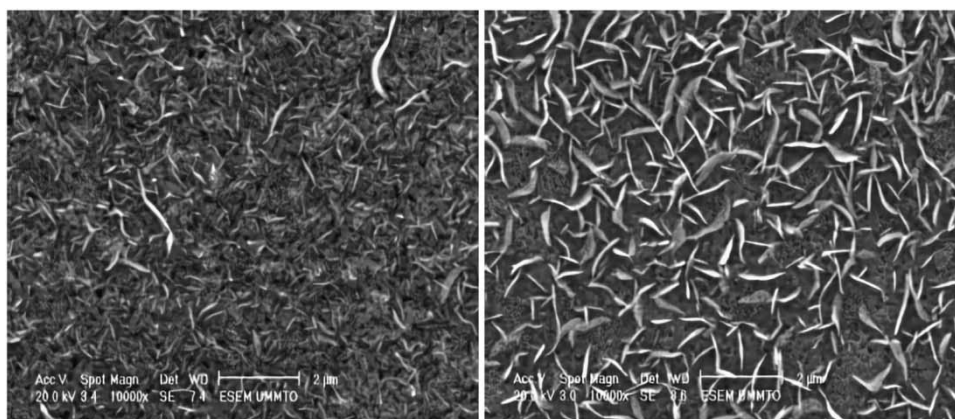

Figure 1 | SEM images of the annealed Fe substrates at 500 °C (2 h, in air), prepared without (left) and with (right) electrochemical pretreatment (0.5 M H$_2$SO$_4$, 6 V, 5 min).
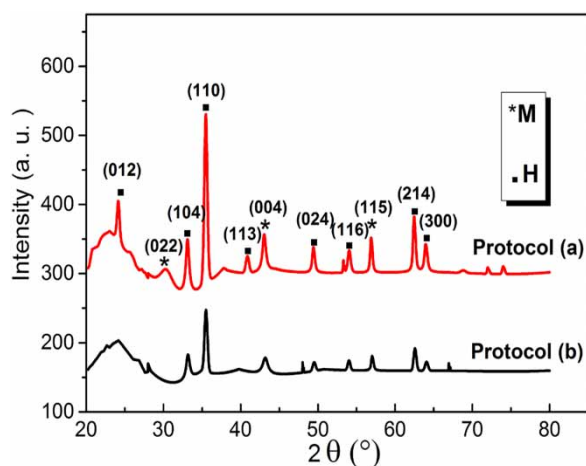
Figure 2 | XRD patterns of hematite prepared by thermal oxidation at 500 °C (2 h, in air), protocol (a) and protocol (b): without and with electrochemical pretreatment (0.5 M H_2SO_4, 6 V, 5 min) respectively.

protocol (a), indicating more compressed crystallites in agreement with others (Bora et al. 2012).

Microstructural analysis

The microstructural investigation consists of exploiting the XRD data to evaluate the average crystallite size (D), microstrain (ε), stress (σ) and dislocation density (δ) of α-Fe_2O_3. The Full Width at Half Maximum (FWHM) (Equation (1)) (Muniz et al. 2016) is a rough way to estimate the crystallite size from the peak broadening (β, rad). The most intense XRD peak and the corresponding average crystallite size (D_{FWHD}) are reported in Table 1. However, a more accurate way to evaluate the crystallite size is to use the Williamson-Hall (W-H) equation (Equation (2)) (Verma et al. 2019), which takes into account the contribution of the crystallite size and lattice strain in the XRD peak broadening:

$$D = \frac{K}{\beta \cos\theta} \qquad (1)$$

$$\beta_{hkl}\cos\theta_{hkl} = \frac{K\lambda}{D} + 4\,\varepsilon\,\sin\theta_{hkl} \qquad (2)$$

Table 1 | Microstructural analysis of the hematite prepared by annealing iron foils at 500 °C (2 h, in air), after surface iron processing according to protocols (a) and (b): without and with electrochemical pretreatment (0.5 M H_2SO_4, 6 V, 5 min), respectively

Sample	D_{FWHM} (nm)	D_{WH} (nm)	ε no unit $\times 10^{-4}$	σ (GPa)$\times$ 10^{-2}	δ (10^{+15} lin.m^{-2})
Protocol (a)	18.49	15.13	−16.07	−38.09	4.37
Protocol (b)	18.08	19.55	−3.02	−7.16	2.62

where K is the shape factor, equal to 0.9, λ the X-ray wavelength (1.540598 Å), and θ_{hkl} is the diffraction angle. The microstrain ε is not in the matrix form because the W-H model is based on the isotropic approximation. B is corrected by using the equation (Equation (3)) (Verma et al. 2019):

$$\beta_{hkl} = \sqrt{\beta_{hkl}{}^2{}_{(measured)} - \beta^2{}_{(instrumental)}} \qquad (3)$$

The microstrain ε and the W-H crystallite size (D_{W-H}) are extracted respectively from the slope and the intercept of the line $\beta\cos\theta$ versus $\sin\theta$. The internal stress σ is deduced from ε as follows (Equation (4)):

$$\sigma = Y\varepsilon \qquad (4)$$

where Y is the Young's modulus (=237 GPa) (Chicot et al. 2011). Similarly, the dislocation density δ, which indicates the density of linear defects in the crystallites, is calculated from the equation (Equation (5)) (Bilgin et al. 2005):

$$\delta = \frac{1}{D^2} \qquad (5)$$

Table 1 summarizes the results of the XRD microstructural analysis; the values of D_{FWHM} are almost the same for both protocols, while D_{W-H} shows a net increase when the electrochemical pretreatment was used. The negative sign of the microstrain (ε) reveals that the α-Fe_2O_3 crystalline structure in both cases is under compressive stress, which is more pronounced with protocol (a). Hence, the surface pretreatment by electrochemical quenching diminishes in a non-negligible manner the compressive stress of the α-Fe_2O_3 structure, reduces the dislocation density, and enhances the crystallite size (Table 1).

Raman analysis

The Raman spectra of α-Fe_2O_3 samples obtained with or without electrochemical pretreatment, respectively protocol (b) and protocol (a), are displayed in Figure 3. The hematite, which belongs to the R-3c space group, has seven symmetrical Raman active modes: 2 A_{1g} and 5 E_g, corresponding to transversal optical vibrations. These expected bands are actually observed at 225 (A_{1g}), 245 (E_g), 291 (E_g), 301 (E_g), 410 (E_g), 498 (A_{1g}) and 613 cm^{-1} (E_g), which is consistent with the results reported in the literature (Lassoued et al. 2017). Additionally, a weak band at 662 cm^{-1} is also
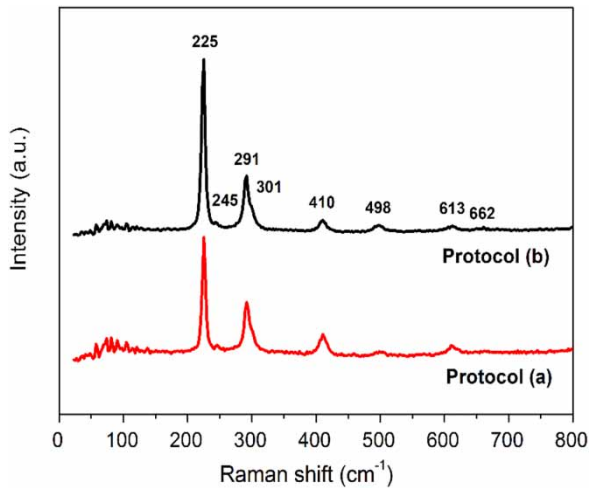
Figure 3 | The Raman spectra of α-Fe$_2$O$_3$ prepared by thermal oxidation in atmospheric air at 500 °C (2 h, in air) using protocol (a) and protocol (b): without and with electrochemical pretreatment (0.5 M H$_2$SO$_4$, 6 V, 5 min), respectively.

detected, whose origin is assigned to an IR-active phonon mode activated by the disorder in the hematite crystal (Jubb & Allen 2010). Moreover, a global blue shift of Raman lines is observed for samples not treated electrochemically and this is indicative of a smaller crystallite size (Jubb & Allen 2010) and/or a higher compressive stress

(McNally 2012), in agreement with previous microstructural results.

Diffuse reflectance

The diffuse reflectance data (Figure 4(a)) of the as-grown α-Fe$_2$O$_3$ films was used to evaluate the gap (E_g), which is a crucial parameter in the photoelectrochemical conversion. Eg is determined according to the Tauc relation (Equation (6)) (Raja *et al.* 2015):

$$(\alpha h\nu)^n = Constant \times (h\nu - E_g) \tag{6}$$

where α is the optical absorption coefficient and $h\nu$ the photon energy, the exponent n depends on the nature of the electronic transition, which takes respectively values of 2 and 0.5 for direct and indirect transition.

Figure 4(b) and 4(c) show the plot of $(\alpha h\nu)^2$ versus $h\nu$; the energy gap can be obtained from the intercept of the linear part of the curve with the energy axis. The optical transition is clearly affected by the pretreatment, as E_g is 1.97 eV for the sample treated electrochemically (protocol b) and increases up to 2.12 eV for the conventional cleaning (protocol a). The smaller gap obtained after the electrochemical treatment is
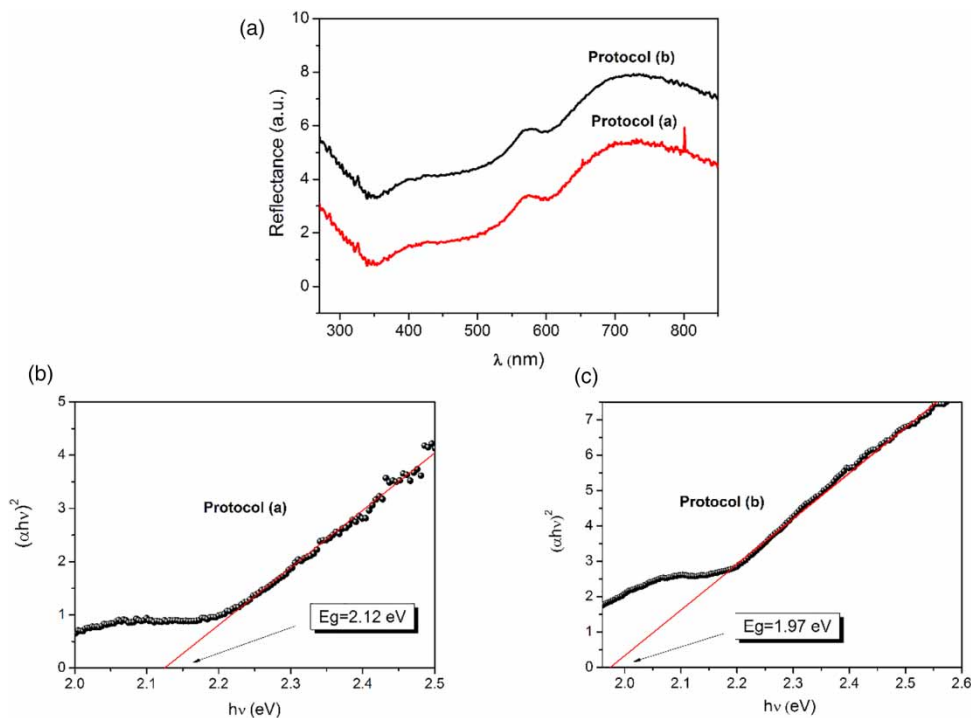

Figure 4 | (a) Diffuse reflectance spectra of the hematite elaborated by thermal oxidation of Fe foils at 500 °C (2 h, in air) for protocols (a) and (b): without and with electrochemical pretreatment (0.5 M H$_2$SO$_4$, 6 V, 5 min) respectively (b) and (c). Determination of the direct band gap is obtained from the intersection of the straight line with energy axis.

presumably related to the larger crystallite size (Pandey et al. 2014), as mentioned above in the microstructural analysis.

Capacitance measurements

In order to determine the role of the pretreatment of Fe sheet on the electronic properties of α-Fe$_2$O$_3$ nanostructures, the interfacial capacitance (C) was measured at the film/electrolyte junction as a function of applied electrode potentials. The measurement was done at a frequency of 10 kHz, a value large enough to ignore the Helmholtz capacity. The variation of the reciprocal square capacitance (C^{-2}) versus the potential (Figure 5) follows the equation (Equation (7)) (Steier et al. 2014):

$$\frac{1}{C^2} = \frac{2}{e\varepsilon\varepsilon_0 A^2 N_A}\left[E - E_{fb} - \frac{k_B T}{e}\right] \qquad (7)$$

e is the electron charge, $\varepsilon = 32$ (Steier et al. 2014) the dielectric constant of the hematite, ε_o the dielectric constant of vacuum (8.85×10^{-12} F m^{-1}), A the surface area (1.2 cm^2), N_A the acceptor density, E_{fb} the flat band potential (vs. SCE), k_B the Boltzmann constant (1.38×10^{-23} J K^{-1}) and T the absolute temperature (298 K).

The acceptor density N_A is evaluated from the slope of the plot (Equation (8)), whose negative value indicates p-type behavior (Figure 5) where the holes are the majority carriers:

$$N_A = \frac{2}{e\varepsilon\varepsilon_0 A^2}\left(d(1/C^2)/dE\right)^{-1} \qquad (8)$$

The values of N_A (6.77×10^{19} cm^{-3}) for protocol (a) and (3.01×10^{20} cm^{-3}) for protocol (b), correspond to an increase by one order of magnitude when electrochemical pretreatment is used. Hematite is commonly an n-type semiconductor, the p-type semiconductivity of as-elaborated α-Fe$_2$O$_3$ is very likely related to the midgap states at the surface. Indeed, near-surface layers generally exhibit a higher deviation from stoichiometry than the bulk; besides, a segregation of intrinsic lattice defects at the surface can occur (Gleitzer et al. 1991). When these midgap surface states are sufficiently high to bring the valence band closer to the Fermi level than the conduction band, the region near the surface turns to p-type and forms an inversion layer (Baca & Ashby 2005).

By eliminating in Equation (7) the term $k_B T$ ($\sim$26 meV at 300 K), since it can be neglected in front of 930 and 770 mV, the straight part of the curve crosses the potential-axis ($C^{-2} = 0$) at the following flat band potentials: $E_{fb} = 0.93$ V$_{/SCE}$ (Figure 5(a)) for protocol (a) and $E_{fb} = 0.77$ V$_{/SCE}$ (Figure 5(b)) for protocol (b). The cathodic shift of E_{fb} toward lower potentials can be related to the increased crystallite size obtained by the electrochemical processing, as observed by Iandolo et al. (2015).

In summary, these results show that the electrochemical pretreatment before thermal oxidation induces changes in the carriers' density as well as on the flat band potential, and thus on the band bending. These electrochemical changes will inevitably impact the photocatalytic properties as will be demonstrated in the next section.

Photoactivity

MB is a cationic dye and α-Fe$_2$O$_3$ has a point of zero charge of 7.9; this suggests beforehand that neutral pH may be beneficial to avoid parasitizing the active photocatalytic sites by
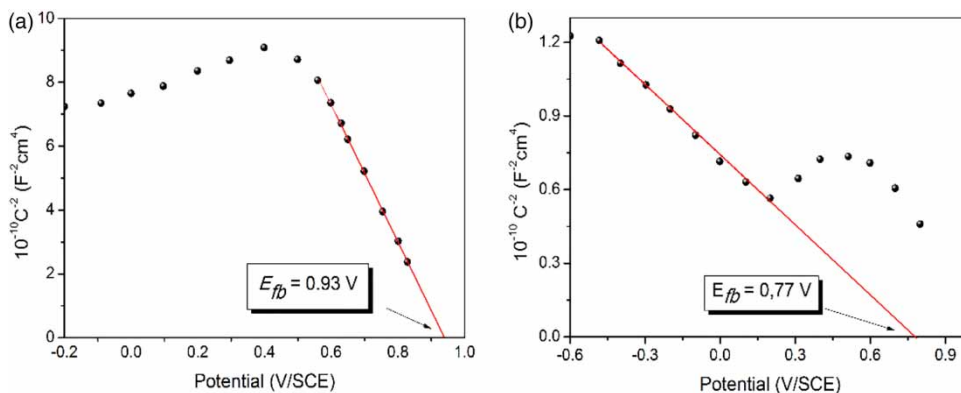

Figure 5 | The Mott-Schottky characteristics of α-Fe$_2$O$_3$ plotted in NaOH (0.5 M) solution at 10 kHz using substrate pretreatment of (a) protocol (a) and (b) protocol (b): without and with electrochemical pretreatment (0.5 M H$_2$SO$_4$, 6 V, 5 min), respectively. The hematite elaboration got by an annealing at 500 °C (2 h) in air atmosphere. Flat band potentials are obtained from the intersection of the straight lines fitting with the potential axis.

a non-desired ionic adsorption. The photoactivity of α-Fe$_2$O$_3$ was successfully tested through the MB degradation at $\sim$ pH 7 under visible-light irradiation; MB is well known for its stability under visible and near UV light. To study the photocatalytic activity of the samples, the pseudo-first order model is used to calculate the rate constant (k_{app}) of MB (Equation (9)). The ratio of the absorbance A_t of MB at time t to A_0 measured at $t = 0$ s must be equal to the concentration ratio C_t/C_o of MB, Equation (10); C_t is the concentration at time t and C_o is the initial concentration. The kinetic is described by the first order model (Amani-Ghadim et al. 2015):

$$\frac{dC_t}{dt} = -k_{app}C_t \tag{9}$$

$$\frac{C_t}{C_0} = e^{-k_{app}t} \tag{10}$$

k_{app} is the apparent rate constant which is obtained from the decrease in peak intensity at 660 nm over time.

Figure 6 shows a decrease in the concentration of MB as a function of time, which indicates the degradation of dye for both protocols (a) and (b). We notice that 78% of MB was degraded within 180 min of visible light irradiation for samples not pretreated (Figure 6(a)) while this degradation reached 84% for the sample electrochemically treated (Figure 6(b)). And it should be pointed out that these MB elimination percentages are linked to photodegradation and not to adsorption, since preliminary tests have shown that elimination by adsorption process does not exceed 8%.

The kinetics of degradation show non-linear variations of C_t/C_0 as a function of time (Figure 7), confirming that the photodegradation kinetic is of the first order. The rate constant k_{app} is equal to 7.37×10^{-3} min^{-1} for the untreated sample and increases up to 8.42×10^{-3} min^{-1} for the electrochemically processed sample.
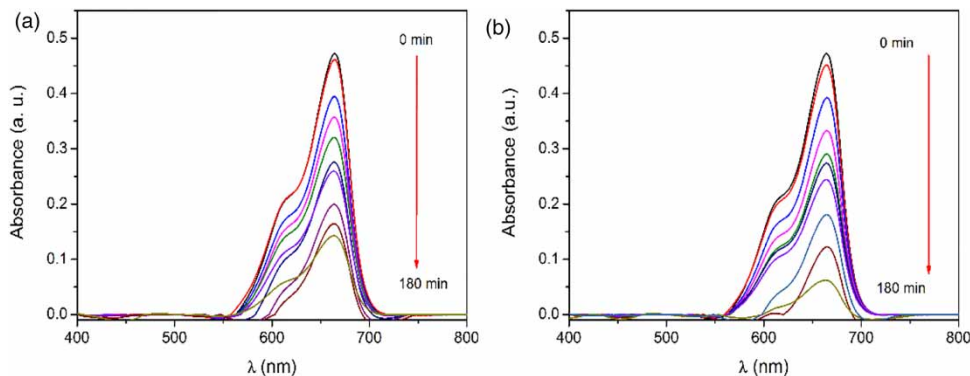

Figure 6 │ Time course UV-Vis absorption spectra evolution of MB photodegradation obtained by irradiation of α-Fe$_2$O$_3$ thin film for protocol (a) and protocol (b): without and with electrochemical pretreatment (0.5 M H$_2$SO$_4$, 6 V, 5 min), respectively. α-Fe$_2$O$_3$ was prepared by thermal oxidation at 500 °C (2 h, in air).
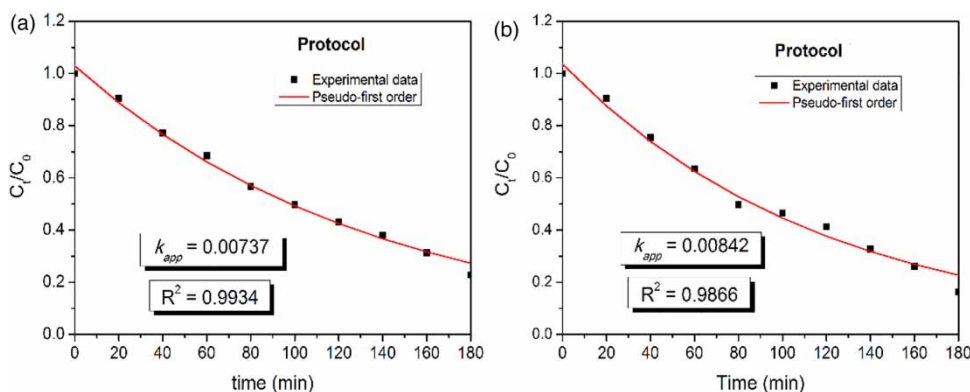

Figure 7 │ Experimental data and fitted non-linear kinetics of MB photodegradation of α-Fe$_2$O$_3$ thin film according to protocol (a) and protocol (b): without and with electrochemical pretreatment (0.5 M H$_2$SO$_4$, 6 V, 5 min), respectively. α-Fe$_2$O$_3$ was prepared by thermal oxidation at 500 °C (2 h, in air).
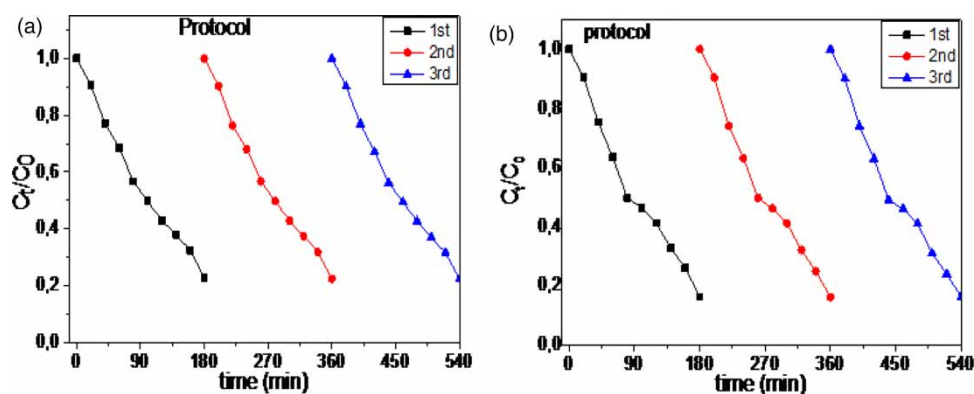
Figure 8 | The kinetics plots of MB photodegradation showing the performance of the α-Fe$_2$O$_3$ thin film after three cycles according to protocol (a) and protocol (b): without and with electrochemical pretreatment (0.5 M H$_2$SO$_4$, 6 V, 5 min), respectively. α-Fe$_2$O$_3$ was prepared by thermal oxidation at 500 °C (2 h, in air).

These results confirm on the one hand that the as-grown nanosheets are effective for the MB degradation if we compare with the literature (Vu *et al.* 2019). On the other hand, the samples submitted to electrochemical pretreatment are more efficient. This better photocatalytic ability is probably due to the higher carrier density, the lower band gap value and the better crystallinity.

Moreover, it is important to mention that the performance of the films does not decrease after the third cycle for both protocols, as is illustrated in Figure 8.

Figure 9 illustrates the photocatalytic process; the efficient photons (energy $>$ E$_g$) are absorbed, causing the electron excitation to the conduction band (CB) leaving a hole in the valence band (VB). Under favorable internal conditions the electrons and holes move in opposite directions

under the effect of the interfacial electric field. They reach the interface electrolyte surface and react respectively with adsorbed O$_2$ and H$_2$O, generating two principal radicals, O$_2^-$ and $\cdot$OH, which mineralize the organic molecule (MB) to CO$_2$ and H$_2$O. This process occurs only by favorable conditions means: high photon absorption, low bulk recombination, reduced surface traps, efficient separation of (e$^-$–h$^+$) pairs and efficient surface charge injection (Tamirat *et al.* 2016).

CONCLUSION

In this work, nanosheets of the hematite α-Fe$_2$O$_3$ were prepared by thermal oxidation of iron foils in air at 500 °C. The iron surface electrochemically pretreated before annealing showed a remarkable influence on the crystallite size, internal stress, surface morphology and optical properties of the hematite. The diffuse reflectance showed that the band gap varies according to the surface pretreatment protocol, from 2.12 eV for a conventional cleaning to 1.97 eV for electrochemical pretreatment. Additionally, the capacitance measurements indicated p-type behavior, with a high hole concentration and a cathodic shift of the flat band for the samples treated electrochemically predicting a better photocatalytic effect. Finally, the photocatalytic study for the methylene blue degradation demonstrated the ability of electrochemical pretreatment to enhance appreciably the photoactivity of α-Fe$_2$O$_3$ nanosheets.

Figure 9 | Scheme of α-Fe$_2$O$_3$ activation under visible light and methylene blue photodegradation.

DATA AVAILABILITY STATEMENT

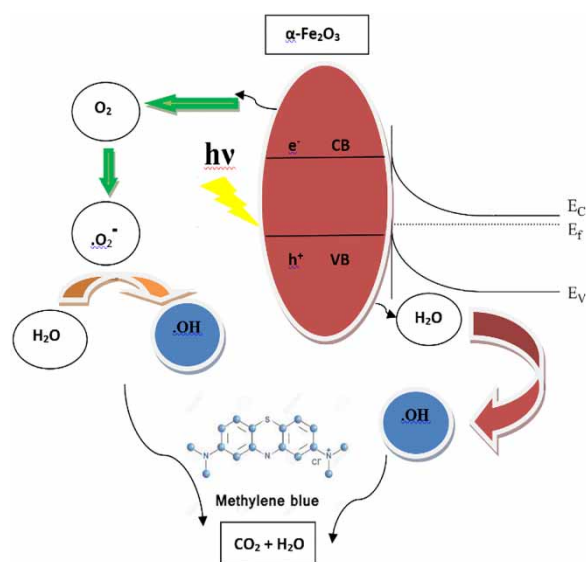All relevant data are included in the paper or its Supplementary Information.

REFERENCES

Amani-Ghadim, A. R., Alizadeh, S., Khodam, F. & Rezvani, Z. 2015 Synthesis of rod-like α-FeOOH nanoparticles and its photocatalytic activity in degradation of an azo dye: empirical kinetic model development. *Journal of Molecular Catalysis A: Chemical* **408**, 60–68. https://doi.org/10.1016/j.molcata.2015.06.037.

Baca, A. G. & Ashby, C. I. H. 2005 *Fabrication of GaAs Devices*. Institution of Electrical Engineers, London, UK.

Bénard, J. & Coquelle, O. 1947 Influence de l'écrouissage provoqué par le travail mécanique à froid sur l'aptitude à l'oxydation du fer. *Revue de Métallurgie* **44** (3–4), 82–86. https://doi.org/10.1051/metal/194744030082.

Bilgin, V., Kose, S., Atay, F. & Akyuz, I. 2005 The effect of substrate temperature on the structural and some physical properties of ultrasonically sprayed CdS films. *Material Chemistry and Physics* **94**, 103–108. https://doi.org/10.1016/j.matchemphys.2005.04.028.

Bora, D. K., Braun, A., Erat, S., Safonova, O., Graule, T. & Constable, E. C. 2012 Evolution of structural properties of iron oxide nano particles during temperature treatment from 250 °C–900 °C: X-ray diffraction and Fe K-shell pre-edge X-ray absorption study. *Current Applied Physics* **12**, 817–825. https://doi.org/10.1016/j.cap.2011.11.013.

Chicot, D., Mendoza, J., Zaoui, A., Louis, G., Lepingle, V., Roudet, F. & Lesage, J. 2011 Mechanical properties of magnetite (Fe_3O_4), hematite (α-Fe_2O_3) and goethite (α-FeO·OH) by instrumented indentation and molecular dynamics analysis. *Material Chemistry and Physics* **129** (3), 862–870. https://doi.org/10.1016/j.matchemphys.2011.05.056.

Chirita, M. & Grozescu, I. 2009 Fe_2O_3-Nanoparticles, physical properties and their photochemical and photoelectrochemical applications. *Chemical Bulletin of 'Politehnica' University of Timisoara* **54** (68), 1–8. Available from: https://www.researchgate.net/publication/228924462_1_Fe_2_O_3-Nanoparticles_Physical_Properties_and_Their_Photochemical_And_Photoelectrochemical_Applications

Cornell, R. M. & Schwertmann, U. 2003 *The Iron Oxides: Structure, Properties, Reactions, Occurrences and Uses*. Wiley-VCH Verlag GmbH & Co. KGaA, Weinheim, Germany.

Elda, R., Tonezzer, A., Orlandi, M., Patel, N., Fernandes, R., Bazzanella, N., Date, K., Kothari, D. C. & Miotello, A. 2017 3D hierarchical nanostructures of iron oxides coatings prepared by pulsed laser deposition for photocatalytic water purification. *Applied Catalysis B: Environmental* **219**, 401–411. https://doi.org/10.1016/j.apcatb.2017.07.063.

Gleitzer, C., Nowotny, J. & Rekas, M. 1991 Surface and bulk electrical properties of the hematite phase Fe_2O_3. *Applied Physics A* **53**, 310–316. https://doi.org/10.1007/BF00357193.

Graat, P. C. J., Somers, M. A. J., Vredenberg, A. M. & Mittemeijer, E. J. 1997 On the initial oxidation of iron: quantification of growth kinetics by the coupled-currents approach. *Journal of Applied Physics* **82** (3), 1416–1422. https://doi.org/10.1063/1.365919.

Hiralal, P., Saremi-Yarahmadi, S., Bayer, B. C., Wang, H., Hofmann, S., Wijayantha, K. U. & Amaratunga, G. A. 2011 Nanostructured hematite photoelectrochemical electrodes prepared by the low temperature thermal oxidation of iron. *Solar Energy Materials and Solar Cells* **95** (7), 1819–1825. https://doi.org/10.1016/j.solmat.2011.01.049.

Iandolo, B., Zhang, H., Wickman, B., Zorić, I., Conibeer, G. & Hellman, A. 2015 Correlating flat band and onset potentials for solar water splitting on model hematite photoanodes. *RSC Advances* **5** (75), 61021–61030. https://doi.org/10.1039/c5ra10215d.

Jubb, A. M. & Allen, H. C. 2010 Vibrational spectroscopic characterization of hematite, maghemite, and magnetite thin films produced by vapor deposition. *Applied Materials & Interfaces* **2** (10), 2804–2812. https://doi.org/10.1021/am1004943.

Lassoued, A., Dkhil, B., Gadri, A. & Ammar, S. 2017 Control of the shape and size of iron oxide (α-Fe_2O_3) nanoparticles synthesized through the chemical precipitation method. *Results in Physics* **7**, 3007–3015. https://doi.org/10.1016/j.rinp.2017.07.066.

Lewis, N. S. & Nocera, D. G. 2006 Powering the planet: chemical challenges in solar energy utilization. *Proceedings of the National Academy of Sciences* **103**, 15729–15735. https://doi.org/10.1073/pnas.0603395103.

McNally, P. J. 2012 *Raman Spectroscopy: Basics and Applications* (S. C. Singh, H. Zeng, C. Guo & W. Cai, eds). pp. 497–510. https://doi.org/10.1002/9783527646821.ch7

Muniz, F. T. L., Miranda, M. A. R., Dos Santos, C. M. & Sasaki, J. M. 2016 The Scherrer equation and the dynamical theory of X-ray diffraction. *ActaCrystallographica Section A* **72** (3), 385–390. https://doi.org/10.1107/S205327331600365X.

Nasibulin, A. G., Rackauskas, S., Jiang, H., Tian, Y., Mudimela, P. R., Shandakov, S. D., Nasibulina, L. I., Sainio, J. & Kauppinen, E. I. 2009 Simple and rapid synthesis of α-Fe_2O_3 nanowires under ambient conditions. *Nano Research* **2**, 373–379. https://doi.org/10.1007/s12274-009-9036-5.

Pandey, B. K., Shahi, A. K., Shah, J., Kotnala, R. K. & Gopal, R. 2014 Optical and magnetic properties of Fe_2O_3 nanoparticles synthesized by laser ablation/fragmentation technique in different liquid media. *Applied Surface Science* **289**, 462–471. https://doi.org/10.1016/j.apsusc.2013.11.009.

Raja, K., Jaculine, M. M., Jose, M., Verma, S., Prince, A. A. M., Ilangovan, K., Sethusankar, K. & Jerome Das, S. 2015 Sol-gel synthesis and characterization of α-Fe_2O_3 nanoparticles. *Superlattices and Microstructures* **86**, 306–312. https://doi.org/10.1016/j.spmi.2015.07.044.

Sivula, K., Le Formal, F. & Grätzel, M. 2011 Solar water splitting: progress using hematite (α-Fe_2O_3) photoelectrodes. *ChemSusChem* **4**, 432–439. https://doi.org/10.1002/cssc.201000416.

Steier, L., Herraiz-Cardona, I., Gimenez, S., Fabregat-Santiago, F., Bisquert, J., Tilley, S. D. & Grätzel, M. 2014 Understanding the role of underlayers and overlayers in thin film hematite photoanodes. *Advanced Functional Material* **24** (48), 7681–7688. https://doi.org/10.1002/adfm.201402742.

Sun, B., Horvat, J., Kim, H. S., Kim, W. S., Ahn, J. H. & Wang, G. 2010 Synthesis of mesoporous α-Fe$_2$O$_3$ nanostructures for highly sensitive gas sensors and high capacity anode materials in lithium ion batteries. *The Journal of Physical Chemistry C* **114** (44), 18753–18761. https://doi.org/10.1021/jp102286e.

Tamirat, A. G., Rick, J., Dubale, A. A., Su, W. N. & Hwang, B. J. 2016 Using hematite for photoelectrochemical water splitting: a review of current progresses and challenges. *Nanoscale Horizons* **1** (4), 243–267. https://doi.org/10.1039/C5NH00098 J.

Verma, K. C., Goyal, N., Singh, M., Singh, M. & Kotnala, R. K. 2019 Hematite α-Fe$_2$O$_3$ induced magnetic and electrical behavior of NiFe$_2$O$_4$ and CoFe$_2$O$_4$ ferrite nanoparticles. *Results in Physics* **13**, 102212. https://doi.org/10.1016/j.rinp.2019.102212.

Vu, X. H., Phuoc, L. H., Dien, N. D., Pham, T. T. H. & Thanh, L. D. 2019 Photocatalytic degradation of methylene blue (MB) over α-Fe$_2$O$_3$ nanospindles prepared by a hydrothermal route. *Journal of Electronic Materials* **48** (5), 2978–2985. https://doi.org/10.1007/s11664-019-07056-2.

Wen, X., Wang, S., Ding, Y., Wang, Z. L. & Yang, S. 2005 Controlled growth of large-area, uniform, vertically aligned arrays of α-Fe$_2$O$_3$ nanobelts and nanowires. *The Journal of Physical Chemistry B* **109**, 215–220. https://doi.org/10.1021/jp0461448.

Yuan, L., Cai, R., Jang, J., Zhu, W., Wang, C., Wang, Y. & Zhou, G. 2013 Morphological transformation of hematite nanostructures during oxidation of iron. *Nanoscale* **5**, 7581–7588. https://doi.org/10.1039/C3NR01669B.